surface mixed-layer age of ~3.5 kyr in the uppermost ~5 cm of the sediments[20]. A contribution of 12% of such surficial material to the total turbidite volume is required to account for the discrepancy between the predicted and measured radiocarbon ages (Table 1). Although it would be possible to obtain the younger age by adding sediments from below the surface mixed layer, any greater depth of erosion would require much larger volumes of sediment because of the short half-life of ^{14}C (5,568 years). The 12% addition adds only 4% to the *E. huxleyi* values, but any greater volume would increase the ratio of *E. huxleyi* significantly beyond the measured values (Fig. 3).

The total volume of turbidite *a* is estimated at 25 km^3, of which 3 km^3 could have been added during transport. It is not possible to determine exactly where the excess surface material would be picked up; this could be around the source area, over the whole transport pathway or irregularly along the pathway. We do not know the width of the flow, but estimate a maximum of ~100 km based on local topography, making the area crossed by the flow less than 70,000 km^2 (Fig. 3). If the sediment was picked up equally over this whole area the average depth of erosion would be about 4.3 cms. It is more likely that this surficial material was eroded soon after the turbidity current was formed, near the source area where accumulation rates are higher and the volume required could be achieved by deeper erosion of a smaller area. The original estimate of an eroded area of 17,000 km^2 must be decreased by 12% to account for the material eroded during flow, and now becomes ~15,000 km^3.

Our micropalaeontological method of age analysis of turbidite mixtures gives estimates of depth and shape of eroded bodies consistent with field data. Comparison of the results with independent ^{14}C dating confirms that the turbidite is composed mainly of sediment from the source area with up to 12% of younger sediment added through erosion of the sea bed during flow of the turbidity current. The micropalaeontological method of assessing the age range of sediment in a turbidite will be applicable to any turbidite where the hemipelagic coccolith record of the source material is known in detail, especially where species abundances change with time. To convert age range to depth of erosion the hemipelagic accumulation rate in the source area must be known, and to determine the area of erosion it is necessary to know the volume of the turbidite. These conditions are most likely to be met in modern deep-sea basins or in ancient basins that have been thoroughly studied. Testing against ^{14}C data will only be possible for turbidites deposited within the past few tens of thousands of years, but should provide valuable data for determining erosion in basins with different geometries, such as steep slopes. □

1. Piper, D. J. W., Shor, A. N., Farre, J. A., O'Connell, S. & Jacobi, R. Geology 13, 538–541 (1985).
2. Heezen, B. C. & Ewing, M. Am. Assoc. Petrol. Geol. Bull. 39, 2505–2514 (1955).
3. Weaver, P. P. E. & Thomson, J. (eds) Geology and Geochemistry of Abyssal Plains (Geol. Soc. Lond. spec. Publ. 31, Blackwell, Oxford, 1987).
4. Simpson, J. E. A. Rev. Fluid Mech. 14, 213–234 (1982).
5. Pantin, H. M. Mar. Geol. 31, 59–99 (1979).
6. Bagnold, R. A. Proc. R. Soc. A265, 315–319 (1962).
7. Parker, G., Fukushima, Y. & Pantin, H. M. J. Fluid Mech. 171, 145–181 (1986).
8. Weaver, P. P. E. & Kuijpers, A. Nature 306, 360–363 (1983).
9. Weaver, P. P. E. & Rothwell, R. G. in Geology and Geochemistry of Abyssal Plains (eds Weaver, P. P. E. & Thomson, J.). 71–86 (Geol. Soc. Lond. spec. Publ. 31, Blackwell, Oxford, 1987).
10. Weaver, P. P. E., Rothwell, R. G., Ebbing, J., Gunn, D. & Hunter, P. M. Mar. Geol. 109, 1–20 (1992).
11. Thomson, J. & Weaver, P. P. E. Sedim. Geol. (in the press).
12. Koopmann, B. "Meteor" Forsch-ergerbn. C35, 23–59 (1981).
13. Weaver, P. P. E. & Hine, N. in Stratigraphic Index of Calcareous Nannofossils (eds A. R. Lord & P. Bown) (British Micropalaeont. Soc. spec. Publ., in the press).
14. Embley, R. W. in Marine Slides and Other Mass Movements (eds Saxov, S. & Nieuwenhuis, J. K.) 189–213 (Plenum, New York, 1982).
15. Bugge, T. Cont. Shelf Inst., Norway, Publ. 110, (1983).
16. Ruddiman, W. et al. Proc. ODP Sci. Res. 108 (Ocean Drilling Program, College Station, Texas, 1989).
17. Thomson, J., Colley, S. & Weaver, P. P. E. Earth planet. Sci. Lett. 90, 157–173 (1988).
18. Erlenkeuser, H. Earth planet. Sci. Lett. 47, 319–326 (1980).
19. Officer, C. B. Mar. Geol. 42, 261–278 (1982).
20. Kershaw, P. J. J. envir. Radioactivity 2, 145–160 (1985).
21. Hoffman, B. W. & van Camerik, S. B. Analyt. Chem. 39, 1198–1199 (1967).
22. Imbrie, J. et al. in Milankovitch and Climate (eds Berger, A., Imbrie, J., Hays, J., Kukla, G. & Saltzman B.) 269–305 (NATO ASI series 1984).
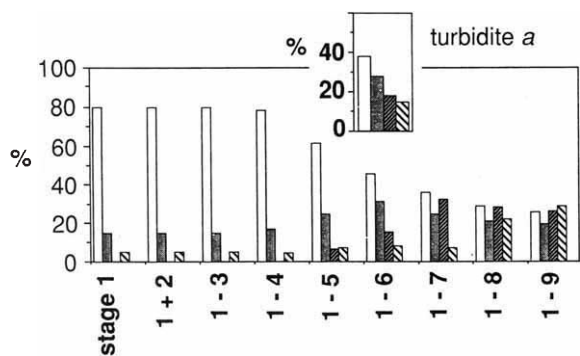
FIG. 3 Synthetic ratios of coccolith species for mixtures incorporating material from oxygen isotope stage 1 only, through to a mixture incorporating all isotope stages from 1–9. For key to shading, see Fig. 2. For each case we have assumed a constant accumulation rate in the source area and equal volumes of material contributed for each time interval (kyr). The synthetic mixtures were created by taking the average values of the species percentages for each isotope stage from Fig. 1 and multiplying these by the length of the stage. For each mixture the appropriate number of isotope stages were added and a new percentage calculated. Inset: Measured ratio of species in turbidite *a* from the Madeira Abyssal Plain. These ratios are very similar to the synthetic mixture of isotope stages 1–6. *P. lacunosa*, common in sediments older than oxygen isotope stage 12 (450 kyr ago) is not present in turbidite *a*, indicating that the turbidite contains only younger material. If 12% of the sediment was added during transport from the surficial layer (as predicted in the text) the ratio of *E. huxleyi* in the mixture of isotope stages 1–6 would increase from 45.5% (main panel) to 49.5%, compared to the measured values of 38% (inset panel).

The displacement field of the Landers earthquake mapped by radar interferometry

Didier Massonnet, Marc Rossi, César Carmona, Frédéric Adragna, Gilles Peltzer*, Kurt Feigl* & Thierry Rabaute†

Centre National d'Etudes Spatiales, 18 Ave. E. Belin, 31055 Toulouse, France
* Observatoire Midi-Pyrénées, 14 Ave. E. Belin, 31400 Toulouse, France
† Scot Conseil, 1 rue Hermes, 31520 Ramonville, France

GEODETIC data, obtained by ground- or space-based techniques, can be used to infer the distribution of slip on a fault that has ruptured in an earthquake. Although most geodetic techniques require a surveyed network to be in place before the earthquake[1–3], satellite images, when collected at regular intervals, can capture co-seismic displacements without advance knowledge of the earthquake's location. Synthetic aperture radar (SAR) interferometry, first introduced[4] in 1974 for topographic mapping[5–8] can also be used to detect changes in the ground surface, by removing the signal from the topography[9,10]. Here we use SAR interferometry to capture the movements produced by the 1992 earthquake in Landers, California[11]. We construct an interferogram by combining topographic information with SAR

images obtained by the ERS-1 satellite before and after the earthquake. **The observed changes in range from the ground surface to the satellite agree well with the slip measured in the field, with the displacements measured by surveying, and with the results of an elastic dislocation model. As a geodetic tool, the SAR interferogram provides a denser spatial sampling (100 m per pixel) than surveying methods[1-3] and a better precision (~3 cm) than previous space imaging techniques[12,13].**

The magnitude 7.3 (M_w) Landers earthquake of 28 June 1992 ruptured over 85 km along a fault system that included the Johnson Valley, Homestead Valley, Emerson, and Camp Rock faults (Fig. 1). Field[11] and seismological[14] investigations show right-lateral slip reaching maxima of 4 m and 6 m, respectively 10 km and 40 km north of the main shock, for which the hypocentral depth[11] was between 3 and 8 km. This event was followed 3 hours later by the Big Bear earthquake (M_w 6.2), for which no surface rupture was reported. Co-seismic horizontal displacements as large as 3 m were measured geodetically and are in good agreement with simple elastic dislocation models[1-3,15]. Near the fault, co-seismic displacements of the order of a metre were detected by pixel correlation of SPOT satellite images[13] and up to 6 cm of post-seismic displacement was observed by surveys in the month following the earthquake[16]. The sequence of earthquakes altered the state of stress on the San Andreas fault system[17,18] and triggered seismicity elsewhere in North America[19].

The ERS-1 satellite passes over the rupture area (Fig. 1) at an altitude of 785 km, transmitting along ray paths pointed west at an average angle of 23° from the vertical. Each SAR image is a map of the ground reflectivity sorted by range, the distance from the radar antenna to the ground. The phase of each 4 by 20 m pixel measures both the range and the phase shift due to reflection of the wave from the ground surface. The latter quantity can be eliminated between two images of the same area if the dielectric characteristics of the ground remain constant and the orbits satisfy the conditions necessary for coherence[6,20]. The remaining path difference, known only to within an integer number of wavelengths, contains information from three sources: (1) relative orbital positions, (2) topography as seen in stereo by the satellite from slightly different orbital passes and (3) any change in position of the ground reflector between the acquisition times of the two images[8,10].

SAR images of the rupture zone were acquired by ERS-1 on four separate dates in 1992: 24 April, 3 July, 7 August, and 11 September. Among the three pairs spanning the earthquake date, the April 24–August 7 pair provides the optimum conditions for image correlation because the orbital separation best meets the coherence condition and the reflective surface was well preserved despite the intervening 105 days.

From these images, we reconstruct the phase of each pixel using a phase-preserving correlator[21]. We adjust the satellite orbital parameters (1) to minimize the number of fringes at the four corners of the image, assuming that the far field displacement is negligible. The stereoscopic path difference (2) is eliminated using a digital elevation model[22]. The interferometric fringes (3) are calculated in the geometry of the radar image and then mapped into the cartographic geometry. There they are resampled on the 90 by 110 m pixels of the elevation model to improve the signal-to-noise ratio.

The resulting interferogram (Fig. 2a and b) is a contour map of the change in range, that is the component of the displacement which points toward the satellite. It includes all the co-seismic and some of the post-seismic deformation. Each fringe corresponds to one cycle, equivalent to 28 mm (half the 56-mm wavelength of the ERS-1 SAR). For the nine geodetic stations located in the coherent part of the interferogram, the range changes are comparable to those calculated from surveying observations of horizontal displacement[1-3] with an r.m.s difference of 1.2 cycles, or 34 mm. This value represents the uncertainty, in an absolute sense, of the range change for a given point in the interferogram, and probably reflects mostly orbital errors.

Figures 2b and c shows two different interferograms of the same area near the fault. Figure 2c was processed in the same way as Fig. 2b, but using a pair of images taken after the earthquake on 3 July and 7 August. Comparison of these two images clearly shows that the fringes in Fig. 2a and b are due to the earthquake. The comparison also indicates that errors in the elevation model propagate into the ranges in Fig. 2a and b at the level of 9 mm, as quantified in the caption. This value represents the uncertainty of the relative change in range between two nearby points in the interferogram.

The co-seismic interferogram (Figs. 2a, 2b and 3a), shows no organized fringes in a band within 5–10 km of the fault trace. In this area, the displacement gradient is sufficiently large that the change in range across a radar pixel exceeds a critical value, and coherence is lost[6,20]. Rotations of small crustal blocks may also reduce the coherence[23]. Indeed, the band of incoherence is not observed in the post-earthquake interferogram (Fig. 2c).

For comparison, we calculate the theoretical change in range (Fig. 3b) using a dislocation model which describes the rupture zone as an elastic half space[15]. The earthquake fault is treated as
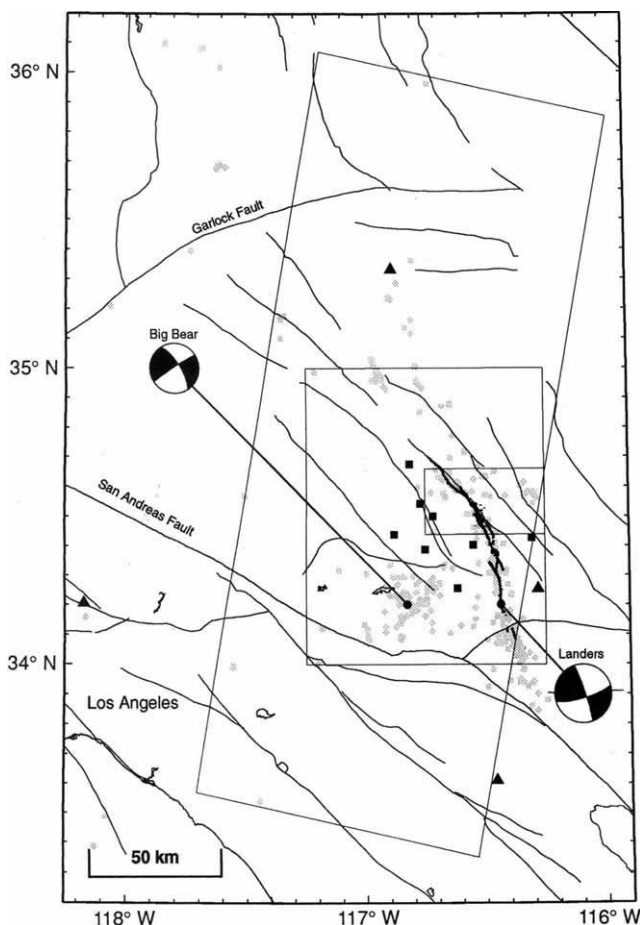
FIG. 1 Active faults in the region of the Landers and Big Bear earthquakes. Heavy solid lines indicate surface rupture associated with the Landers event[11]. No surface break was reported for the Big Bear event. Solid circles are epicentres[11] of Landers and Big Bear main shocks with focal mechanisms (G. Ekström and M. Salganik, personal communication). Gray spots are earthquakes with magnitude greater than 3 between 25 June and 8 August 1992. Rectangles denote the areas covered by Fig. 2a (large), Fig. 2b and c (small) and Fig. 3a and b (medium). Squares and triangles denote geodetic stations where the co-seismic displacement has been estimated by the U.S. Geological Survey[3] and the Permanent GPS Geodetic Array[1,2], respectively.

eight vertical planar segments which represent the surface rupture and the aftershock distribution[11]. Each segment is subdivided into rectangular patches 2 km in length. For the Landers event, the slip on each patch matches the offset mapped in the field (K. Hudnut, personal communication, published in ref. 14). The modelled rupture extends from 0 to 15 km below the surface, to match the moment[11] of 10^{20} N m. For the Big Bear event, where no surface rupture was observed, the model includes the geometry from previous studies[1,2], a simple triangular slip distribution extending from 3 to 15 km below the surface, and a moment[2] of 4×10^{18} N m.

The outstanding resemblance between the modelled and observed fringe patterns, which were obtained independently, validates both calculations. They agree to within two fringes (56 mm) in both the near and far field. Larger, but local, differences within 10 km of the fault are due to the simple discretization of the elastic model. The large lobes are adjacent to the central section of the fault, where the maximum slip was observed[11]. On both sides of the fault, the fringes converge toward points where the fault slip vanishes. This occurs at both ends of the fault and 20 km north of the epicentre, between the two main ruptures[11,14].

The modelled and observed changes in range agree to within 30 mm in a profile perpendicular to the central section of the fault (Fig. 4a). The agreement in the decay of displacement with distance out to 40 km from the fault suggests that the rupture depth of 15 km in the model is correct in this section of the fault. The right-lateral slip on the fault can be estimated from the
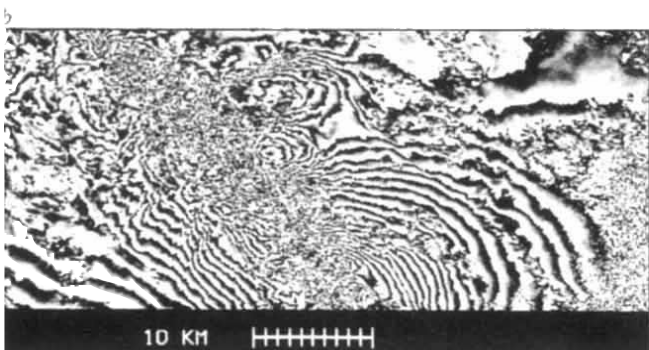

FIG. 2 a, Post-processing interferometric fringes obtained with the pair of ERS-1 SAR images taken before (24 April) and after (7 August) the earthquake. The image covers the 125 by 275 km area outlined by the large rectangle in Fig. 1. One cycle of gray shading represents a range difference of 28 mm between the two images. It is a measure of the component of the displacement vector which points toward the satellite. The number of fringes increases from zero at the northern edge of the image, where no co-seismic displacement is assumed, to at least 20 (representing 560 mm in range difference) in the cores of the lobes adjacent to the fault. The asymmetry between the two sides of the fault is due to the curvature of the fault and the geometry of the radar. Displacements with different azimuths on opposite sides of the fault produce different fringe patterns because the radar resolves only the range component of the displacement vector. b, Detail of the fringe map in a, covering an area 64 km by 33 km as outlined by the small rectangle in Fig. 1. The orbital separation, or baseline, between the images taken 24 April and 7 August measures approximately 60 m and 126 m, in the vertical and horizontal components respectively. These values imply that an error in the elevation model of 72 m would produce a shift of one full cycle. c, Fringes obtained using the same processing and area for b, but with SAR images acquired on 3 July and 7 August (after the 28 June earthquakes). The maximum post-seismic displacement observed[16] in the area and time covered by this image pair is 4 cm, which would produce a change in range of less than 0.2 cycles. The fringes are apparently due to errors in the elevation model because the interferogram exhibits characteristic topographic fringes and local incoherence in areas of high relief[20]. The orbital separation of this pair of images measures 22 m and 496 m in the vertical and horizontal components, respectively. These values imply that an error of 16 m in the elevation model would create one fringe. This interferogram is thus 4.5 times more sensitive to such errors than the co-seismic image pair (a and b). Since this post-seismic image pair (c) exhibits a noise level of about 1.5 cycles, we infer about 24 m of noise in the elevation model, in agreement with the published uncertainty[22] of 30 m. This noise level would in turn contribute about one third of a cycle, or 9 mm to the range changes in the co-seismic interferogram (a and b).
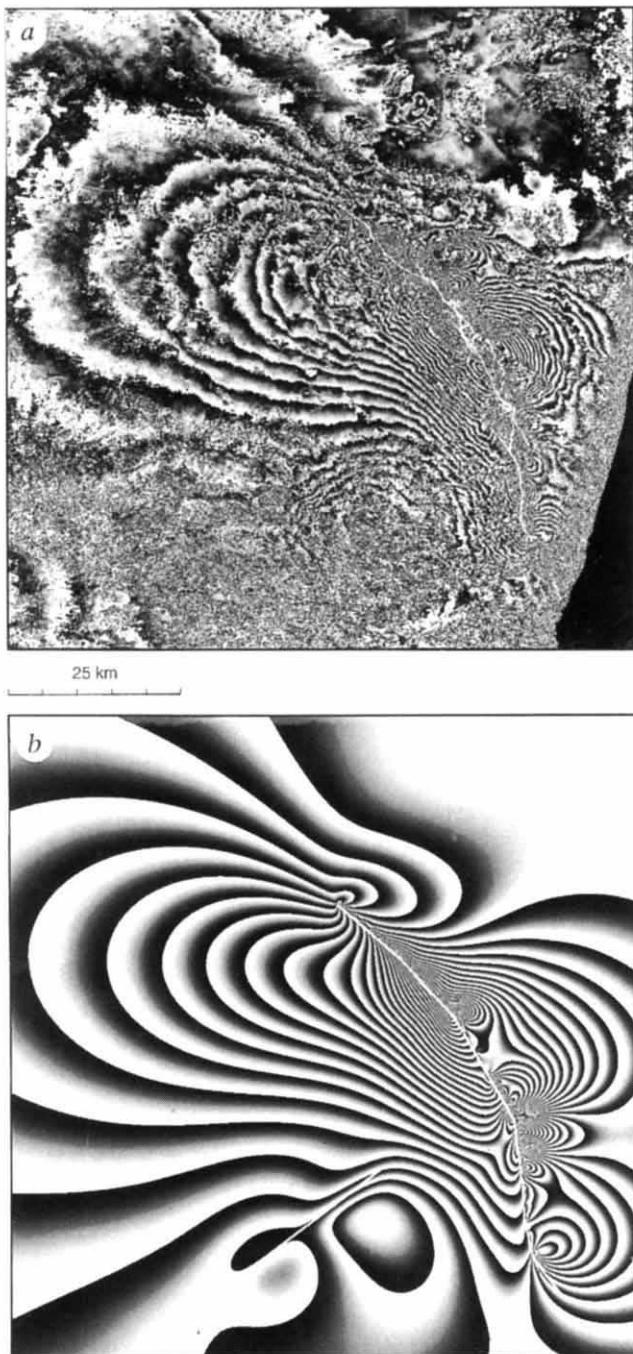
25 km
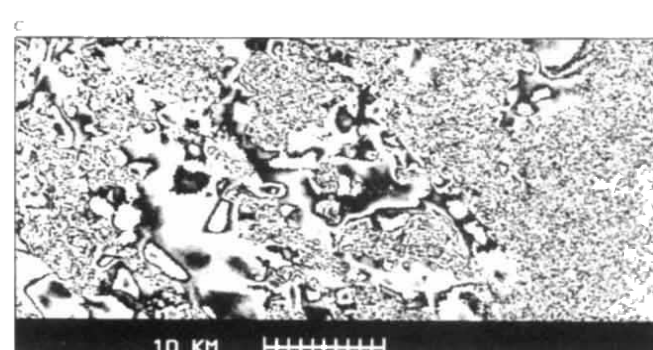
FIG. 3 *a*, Detail of the earthquake area showing the same interferogram as in Fig. 2 and *b* a synthetic interferogram calculated with an elastic half-space dislocation model as described in the text. One cycle of gray shading represents 28 mm of change in the range, as in Fig. 2*a* and *b*. White segments depict the fault geometry as mapped in the field[11] (*a*), and as used in the model (*b*). Both images cover the 90 by 110 km area outlined by the medium rectangle in Fig. 1. The observed (*a*) and modelled (*b*) fringe patterns differ mostly in the short-wavelength features near the rupture zone. These local concentrations of strain occur at the ends of fault segments. They are highly sensitive to the detailed geometry of the fault (*a*) and poorly explained by the simple geometry adopted in the model (*b*). The band of incoherence in the rupture zone (*a*) is delimited in many places by two parallel fault splays. These areas are also affected by intense secondary faulting, especially along the northern and southern parts of the Homestead Valley fault[11]. The loss of correlation might be explained by a large displacement gradient imposed by slip on these secondary faults and possibly rotation of blocks between them.

interferogram by assuming that the observed change in range is due only to horizontal right-lateral strike slip on a plane trending N20°W. The estimated slip (see Fig. 4*b* and associated caption) agrees in magnitude and general distribution with the field observations[11].

The Landers earthquake, because of its large and clear surface rupture, provides a positive validation of the use of radar interferometry for measuring co-seismic displacements. Changes in range have been estimated under realistic conditions including actual topography and unexceptional orbits. The resulting map of the displacement field is unprecedented in its combination of precision (34 mm) and dense spatial sampling (100 m per pixel). These attributes could be refined with an improved elevation model and a more precise orbital calcula-
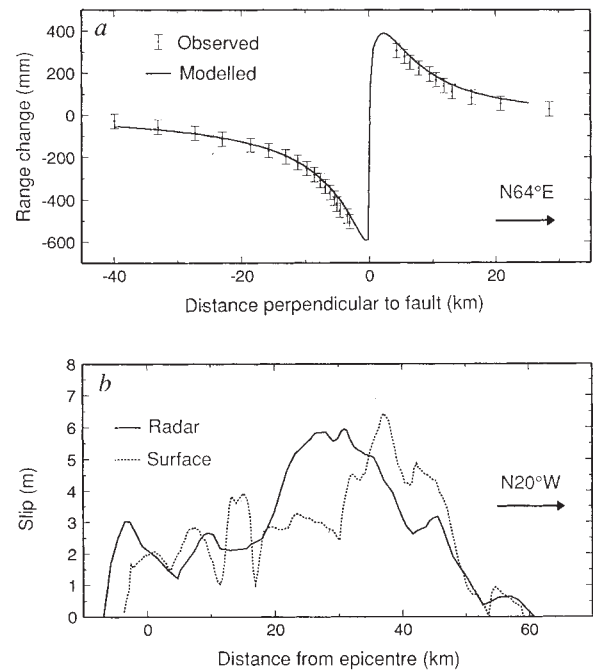

FIG. 4 *a*, Comparison of the co-seismic change in range as observed (points with error bars) and modelled (solid line) along a profile striking N64°E perpendicular to the fault trace at 34.44° N, where the maximum slip was observed[11]. The observed values are estimated by integrating the phase difference in Fig. 2*a* along the profile. The level of the observed values west and east of the fault is determined by counting fringes along a closed path passing north of the incoherent band in the rupture zone. The origin, with zero change in range, is taken to be where the path crosses the black-to-white fringe contour emanating from the northernmost part of Fig. 2*a*, where we assume no co-seismic displacement. *b*, Comparison of slip distribution along the fault estimated by integration of interferometric fringes (solid line) and from field measurements[11] of surface rupture (dashed line). Both quantities are projected onto a line striking N20°W and distance is reckoned positive to the north of the main shock epicentre (34.20° N, 116.44° W). Fringes are counted along two profiles following the western and eastern edges of the incoherent band, at a distance of 5–10 km from the fault. The fringes are extrapolated across the band of incoherence by projecting them in a direction perpendicular to the N20°W strike of the fault. Horizontal slip is derived from the measured slant-range displacement by assuming purely horizontal, right-lateral strike-slip displacement on the N20°W trend. In this approximation, the ratio between slant-range and horizontal slip is the product $\sin\alpha\sin\phi$, where α is the angle between the fault and the satellite nadir ground track and ϕ is the radar incidence angle. The apparent offset of 10 km between the maxima of the two curves results from the right-angle projection of fringes which appear to intersect the fault at an oblique angle. The interferometric estimate of slip does not show all the short wavelength features of the field estimate because the slip on the fault is inferred by extrapolating slip observed at points away from the fault.

141

tion. Displacements of 1 cm have been detected for artificial targets[24,25] and the ultimate precision of the technique is at the millimetre level[26]. For this shallow earthquake, the range changes measured by radar agree extremely well with both the field observations at the fault and the dislocation model in the intermediate and far fields. The detailed features of the radar fringes near the fault require more sophisticated modelling. For deeper earthquakes associated with little or no surface rupture, radar interferometry will become a powerful tool for measuring surface displacement in the intermediate and far fields. Unlike surveying techniques, there is no need to install ground stations before the earthquake. To ensure a pre-earthquake observation, one needs only to archive radar images of the potentially seismogenic area each time the satellite passes over it, as ERS-1 currently does once every 35 days. □

1. Blewitt, G. et al. Nature 361, 340–342 (1993).
2. Bock, Y. et al. Nature 361, 337–340 (1993).
3. Murray, M. H., Savage, J. C., Lisowski, M. & Gross, W. K. Geophys. Res. Lett. 20, 623–626 (1993).
4. Graham, L. C. Proc. Inst. elect. electron. Engrs 62, 763–768 (1974).
5. Zebker, H. & Goldstein, R. J. geophys. Res. 91, 4993–5001 (1986).
6. Gabriel, A. K. & Goldstein, R. M. Int. J. Remote Sensing 9, 857–872 (1988).
7. Li, F. K. & Goldstein, R. M. IEEE Trans. Geosci. Remote Sensing 28, 88–97 (1990).
8. Massonnet, D. Proc. int. Geophys. appl. Remote Sensing Symp. 2, 1431–1434 (1990).
9. Massonnet, D. Etude de Principe d'une Détection de Mouvements Tectoniques par Radar Internal memo No. 326 (Centre Nationale d'Etudes Spatiales, Toulouse, 1985).
10. Gabriel, A. K., Goldstein, R. M. & Zebker, H. A. J. geophys. Res. 94, 9183–9191 (1989).
11. Sieh, K. et al. Science 260, 171–176 (1993).
12. Crippen, R. E. Episodes 15, 56–61 (1992).
13. Crippen, R. E. & Blom, R. G. Eos (Supplement, 27 Oct.) 73, 364 (1992).
14. Kanamori, H., Thio, H.-K., Dreger, D. & Hauksson, E. Geophys. Res. Lett. 19, 2267–2270 (1992).
15. Okada, Y. Bull. seism. Soc. Am. 75, 1135–1154 (1985).
16. Shen, Z., Jackson, D., Feng, Y., Kim, M. & Cline, M. Bull. seism. Soc. Am. (submitted).
17. Jaumé, S. C. & Sykes, L. R. Science 258, 1325–1328 (1992).
18. Stein, R. S., King, G. L. P. & Lin, J. Science 258, 1328–1332 (1992).
19. Hill, D. P. et al. Science 260, 1617–1623 (1993).
20. Massonnet, D. & Rabaute, T. IEEE Trans. Geosci. Remote Sensing 31, 455–464 (1993).
21. Massonnet, D., Rossi, M. & Adragna, F. Paper presented at PRISME, CEOS workshop on SAR calibration, Oberpfaffenhofen, Germany, October 9–11 (1991).
22. Elassal, A. A. & Caruso, V. M. USGS Digital Cartographic Data Standards: Digital Elevation Models (National Cartographic Information Center, Reston, 1984).
23. Zebker, H. A. & Villasenor, J. IEEE Trans. Geosci. Remote Sensing 30, 950–959 (1992).
24. Cafforio, C., Prati, C. & Rocca, F. IEEE Trans. aero. Elect. Syst. 27, 194–207 (1991).
25. FRINGE SAR Interferometry Working Group, Proceedings of First Workshop, 12 Oct. 1992, Frascati, Italy (1992).
26. Gray, A. L. & Farris-Manning, P. J. IEEE Trans. Geosci. Remote Sensing 31, 180–191 (1993).

The tropics as a source of evolutionary novelty through geological time

David Jablonski

Department of the Geophysical Sciences, University of Chicago, 5734 South Ellis Avenue, Chicago, Illinois 60637, USA

SPATIAL and temporal variations in biological diversity can be shaped by a variety of dynamical interactions between origination and extinction[1–3]. For this reason, the evolutionary basis of the latitudinal diversity gradient—with the tropics extraordinarily rich in species, higher taxa and evolutionary novelties—has been much debated[4–8]. High origination rates with the tropics operating as a diversity pump[8–11], low extinction rates with the tropics operating as a diversity accumulator[12–15], or some combination of the two[16–18], have all been proposed to explain the wealth of higher taxa and morphological variety in low latitudes. Few historical data have been available, however, to test directly whether the tropics are 'a cradle or a museum'[15,19]. A new palaeontological analysis of post-Palaeozoic marine orders shows significantly more first appearances in tropical waters, whether defined latitudinally or biogeographically, than expected from sampling alone. This provides direct evidence that tropical regions have been a major source of evolutionary novelty, and not simply a refuge that accumulated diversity owing to low extinction rates.

Forty-two orders of benthic marine invertebrates have appeared since the beginning of the Mesozoic[20–22], and the age, environment, and location of the oldest known members are documented[20]. These data are difficult to evaluate, however, because palaeontological sampling is severely biased geographically, with maximum density in north temperate latitudes[23–25]. First occurrences of the 26 orders considered to have good preservation potential[20] were restored to their original palaeolatitudes, grouped in 10° belts (Fig. 1a), and compared to two null hypotheses that quantify different aspects of sampling bias:

$H_0 1$: Observed first appearances are determined primarily by preservational factors. This distribution (Fig. 1c) was based on the first occurrences of orders whose members are only lightly mineralized or easily disarticulate into seldom identified fragments. These records of poorly preserved orders are probably

dictated more by vagaries of sampling and preservation than by true biogeographic history, and thus provide one measure of the distribution or discovery rate of deposits yielding especially rich biotas[20].

$H_0 2$: Observed first appearances are determined primarily by sampling intensity. This distribution (Fig. 1d) was based on all published records of echinoid species (excluding isolated spines) from the beginning of the Triassic to the Bajocian Stage of the Middle Jurassic, an interval that encompasses over half of the ordinal originations[26]. Echinoids are relatively common post-Palaeozoic fossils that have attracted considerable palaeontological attention over the past 200 yr, so that the geographic pattern of their individual records provides a general measure of sampling intensity across latitude. Because many of the well-preserved orders[20] are in Phylum Echinodermata, echinoids are probably a more appropriate taphonomic control[20] than molluscs or other taxa.

First occurrences of the well preserved orders (Fig. 1a, b) are significantly more frequent in tropical seas relative to either of the null hypotheses (Fig. 1c, d). The Early Triassic is especially poorly sampled and poorly understood biogeographically[20,27], but results remain significant even when originations in this interval are excluded.

Adjustment of the well preserved ordinal occurrences using $H_0 1$ and $H_0 2$ datasets (Fig. 1e, f) gives a general picture of how far the well preserved orders diverge from null expectations. These can only be very approximate corrections but serve to illustrate, for example, that so few poorly preserved orders and species records occur at 0–20° palaeolatitude that even the low number of well preserved orders appearing there exceeds that expected from sampling. More generally, the relatively wide distribution of first occurrences in Fig. 1a and 1b, despite the massive sampling biases revealed in Fig. 1c and 1d, suggests that improved sampling would shift even more ordinal originations into tropical regions. Also, because comparisons are made within each 10° band, the decrease in global surface area with increasing latitude is factored out as a potential bias.

The distribution of reefs and other indicators of tropical conditions has oscillated continually over geological time[28,29], so that first occurrences might better be calibrated not to absolute palaeolatitude but to the contemporaneous limits of tropical biotas. Such a biogeographic calibration yields results comparable to the palaeolatitudinal tests (Fig. 2): well preserved orders first occur in tropical settings significantly more frequently than